



ASME Journal of Fluids Engineering Online journal at:

https://asmedigitalcollection.asme.org/fluidsengineering



S. M. Mahbobur Rahman²

Department of Mechanical Engineering, Virginia Tech, Norris Hall, Room 107, 495 Old Turner Street, Blacksburg, VA 24061 e-mail: mahbobur@vt.edu

Rohith Warrier

Department of Mechanical Engineering, Virginia Tech, Norris Hall, Room 107, 495 Old Turner Street, Blacksburg, VA 24061 e-mail: rohithwarrier@vt.edu

Alexandrina Untaroiu

Associate Professor Department of Mechanical Engineering, Virginia Tech, Norris Hall, Room 324, 495 Old Turner Street, Blacksburg, VA 24061 e-mail: alexu@vt.edu

Christopher R. Martin

Associate Professor Department of Mechanical Engineering, Altoona College, Penn State University, Eiche Library, 3000 Ivyside Park, Room 145, Altoona, PA 16601 e-mail: crm28@psu.edu

Simulating the Effect of Electric Bias Voltages on the Electrical Characteristics of Oxyfuel Preheat Flame Using Reduced Combustion Mechanism¹

A three-dimensional computational model is presented in this paper that illustrates the detailed electrical characteristics, and the current-voltage (i-v) relationship throughout the preheating process of premixed methane-oxygen oxyfuel cutting flame subject to electric bias voltages. As such, the equations describing combustion, electrochemical transport for charged species, and potential are solved through a commercially available finite volume computational fluid dynamics (CFD) code. The reactions of the methane-oxygen (CH₄ $-O_2$) flame were combined with a reduced mechanism, and additional ionization reactions that generate three chemi-ions, H_3O^+ , HCO^+ , and e^- , to describe the chemistry of ions in flames. The electrical characteristics such as ion migrations and ion distributions are investigated for a range of electric potential, $V \in [-5V, +5V]$. Since the physical flame is comprised of twelve Bunsen-like conical flames, inclusion of the third dimension imparts the resolution of fluid mechanics and the interaction among the individual cones. It was concluded that charged "sheaths" are formed at both torch and workpiece surfaces, subsequently forming three distinct regimes in the i-v relationship. The i-v characteristics obtained from this study have been compared to the previous experimental and two-dimensional computational model for premixed flame. In this way, the overall model generates a better understanding of the physical behavior of the oxyfuel-cutting flames, along with more validated i-v characteristics. Such understanding might provide critical information toward achieving an autonomous oxyfuel-cutting process. [DOI: 10.1115/1.4062963]

Keywords: oxyfuel flame, electrical characteristics, preheating process, bias voltages, CFD, i-v relationship

Introduction

Due to the design restrictions imposed by the very benefits that prompt many manufacturers to choose the oxyfuel flame-cutting technique over its more sophisticated competitors such as laser, plasma, and water jet cutting, it is difficult to find a sensor suite suitable for fully automating a mechanized system. Despite challenges with fully automating the procedure, oxyfuel cutting has maintained its global relevance over the century since it was widely embraced as a favored method for cutting thick metallic surfaces. In this procedure, the metallic work parts are heated by the cutting torches using a premixed fuel-oxygen gas mixture so that they can be chemically cut by a high-velocity stream of pure oxygen.

A pictorial illustration of the cross-sectional arrangement of an oxyfuel preheat flame is shown in Fig. 1.

Nevertheless, the mechanized oxyfuel-cutting process has never profited from autonomy because of the limits of existing sensing technology at high-temperature operating conditions. As a result, an experienced labor force is necessary to operate the system, diminishing the efficacy of this cutting procedure.

Initial studies [1–6] have shown that certain electrical events connected with the flame itself, known as "ion currents", can accurately signal vital process conditions. These findings have provided the impetus for a potential solution to this problem. Provided that an autonomous process is achieved, this work could realize reliable cost-effective control of the oxyfuel cutting process. This capability is of great interest to many core US industries involved in construction, as well as major equipment manufacture for defense and energy applications.

Due to the chemi-ionization process, it is well recognized that high-temperature reaction zones in flames carry electricity [7,8]. Extensive research was conducted into the chemical mechanisms responsible for the generation and recombination of these ions in flames [8–10]. The current–voltage $(i-\nu)$ relationship with various

 $^{^1\}mathrm{Paper}$ presented in part at the IMECE 2022, October 30–November 3, 2022, Columbus, OH, Paper No. IMECE2022-95787.

²Corresponding author.

Contributed by the Fluids Engineering Division of ASME for publication in the JOURNAL OF FLUIDS ENGINEERING. Manuscript received February 15, 2023; final manuscript received July 7, 2023; published online August 8, 2023. Assoc. Editor: Emily Ryan

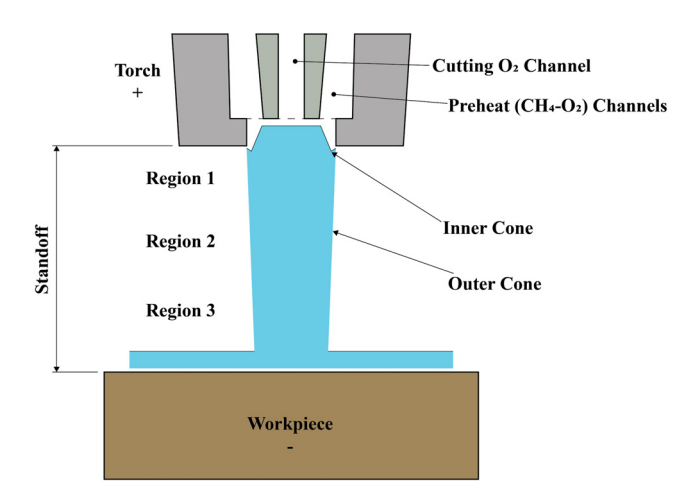


Fig. 1 Cross-sectional arrangement of oxyfuel preheating flame

critical parameters (such as standoff, flow rate, and fuel-oxygen ratio) of an oxyfuel flame has been identified as the most important electrical feature under an electric field during the preheating process in previous works [11–13]. Belhi et al. [14] found a link between (strong) electric fields and flame standoff distance and stability. Fialkov [10] provided an in-depth summary of the studies undertaken on ionized flames. It has been shown that when a voltage is introduced between the torch and the workpiece, the i-v curve splits into three separate regimes [15]. Additional research into the i-v curves has shed light on the rate of formation of charged species [16,17] and the impact of electric fields on flames [1,18–20].

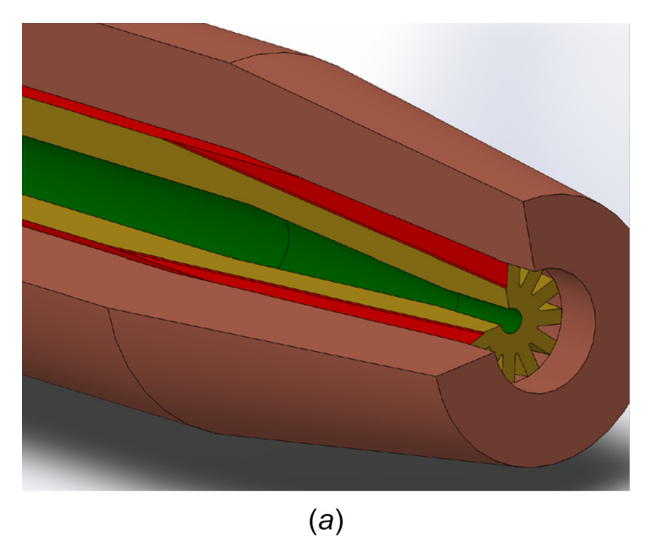
Martin et al. have conducted a number of experimental studies over the years to determine the viability of automated oxyfuel cutting sensors [1,2], and to quantify the electrical signatures in oxyfuel flame [3,21]. To further elucidate the experimental results and to investigate the electrical characteristics such as ion migrations and ion distributions, a comprehensive two-dimensional computational simulation was completed using only the reduced combustion chemical mechanism with ion-exchange reactions [4,22]. Nonetheless, the findings exhibit some magnitude of differences from the experimental results [1,15].

This study aims to analyze and quantify the electrical features of the oxyfuel flame preheating process, as well as to emphasize the constructive comparisons between the numerical and experimental results, by developing a comprehensive three-dimensional (3D) computational model. As a whole, this work will illustrate the specific electrical properties of a premixed methane-oxygen oxyfuel preheat flame when exposed to an electric field. Since the physical flame is made up of twelve (12) Bunsen-like conical flames, including a third dimension will lead to better comprehending offluid dynamics and the interaction among the individual cones. The current computational model provides not only a better understanding of the physical behavior of the oxyfuel-cutting flames but also the means to construct a more realistic *i*–*v* relationship.

Materials and Methods

Geometry. Figure 2 depicts a pictorial view of an oxyfuel-cutting torch [6]. The preheat channels in Fig. 2(a) supply the premixed fuel (CH₄) and oxygen (O₂) mixture via twelve (12) triangular passages. The cutting oxygen passage in the center was not used, indicating that no cutting oxygen is used at this stage. This is known as the oxyfuel flame cutting process's preheating stage.

Figure 3 provides an illustration of the geometry behind the concept of a 15 deg wedge model that represents half of a triangular opening (Fig. 2(a)). This is equivalent to 1/24th of the section that deals with the physical setup and the work surface. Premixed fuel (CH₄) and oxygen (O₂) are introduced through an imaginary annular



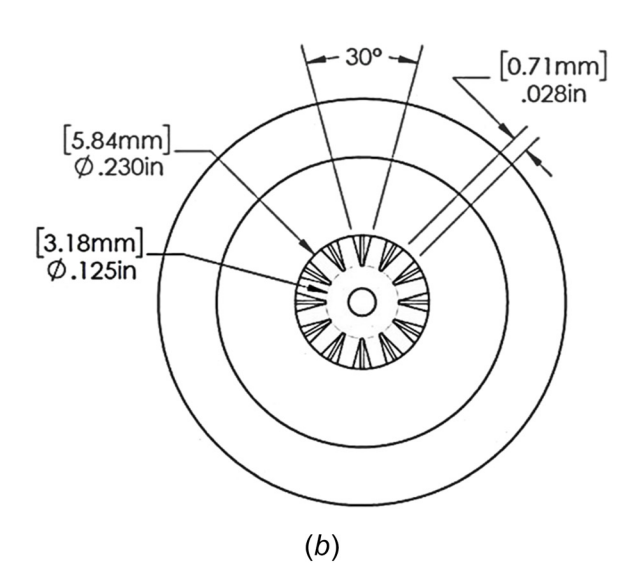


Fig. 2 Oxyfuel cutting torch profile [6]: (a) torch tip and (b) torch tip dimensions

slot labeled as an inlet. The bottom triangular wedge symbolizes the work surface, while the white-colored surfaces (conformal—front and rear) reflect the assembly's periodic rotation. There is a fixed height of $12\,\mathrm{mm}~(\approx 0.5\,\mathrm{in.})$ between the torch and the work surface. Boundary conditions for walls are imposed on the remaining surfaces, whereas the gray ones are interpreted as openings.

Governing Equations. The conservation equations for reacting flows in the presence of electric bias voltages regulate the problem under investigation. This includes the conservation equations for mass, momentum, total energy, and species mass fractions, as derived in Ref. [23]. One very recent illustration of this can be seen in the work of Ref. [24]

$$\nabla \cdot (\rho U) = 0 \tag{1}$$

$$\nabla \cdot [\rho \mathbf{U}\mathbf{U} + pI - \tau] = 0 \tag{2}$$

$$\nabla \cdot \left[\left(\rho U \left(E + \frac{U.U}{2} \right) \right) + (pI - \tau) \cdot U + q \right] = 0$$
 (3)

$$\nabla \cdot [\rho UY_i + J_i] = \dot{\omega}_i, \quad i = 1, 2, ..., N - 1$$
 (4)

The density (ρ) , velocity vector (U), total energy (E), and mass fraction (Y_i) for N reacting species are calculated by solving

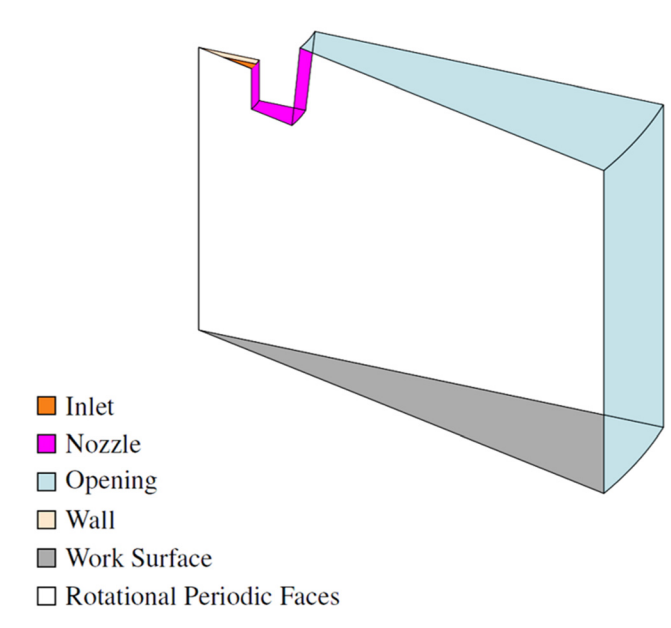


Fig. 3 Three-dimensional 15 deg wedge model

Eqs. (1)–(4). Since the gas is assumed to be ideal, the pressure, p, is determined using the equation of state

$$\rho = \frac{p}{R_u T \sum_{i=1}^{N} \frac{Y_i}{MW_i}} \tag{5}$$

The stress tensor τ and mass diffusion J_i are defined as

$$\tau = \left[(\nabla U + \nabla U^T) - \frac{2}{3} \nabla \cdot \mathbf{U} \mathbf{I} \right] \tag{6}$$

$$J_{i} = -\left(\rho D_{i,m} + \frac{\mu_{t}}{\rho D_{t}}\right) \nabla Y_{i} - D_{T,i} \frac{\nabla T}{T}$$
 (7)

where I is the identity tensor, Sc_t is the turbulent Schmidt number $(=\frac{\mu_t}{\rho D_t})$. Here, μ_t is the turbulent viscosity and D_t is the turbulent

The realizable $\kappa - \varepsilon$ turbulence model [25] was chosen given the turbulent nature of the flow inside the domain. The transport equations for κ and ε in the realizable $\kappa - \varepsilon$ model are

$$\frac{\partial}{\partial t}(\rho k) + \nabla \cdot (\rho k U) = \nabla \cdot \left[\left(\mu + \frac{\mu_t}{\sigma_k} \right) \nabla k \right] + G_k + G_b - \rho \varepsilon$$

$$- Y_M + S_k \tag{8}$$

$$\begin{split} \frac{\partial}{\partial t}(\rho k) + \nabla \cdot (\rho \varepsilon U) &= \nabla \cdot \left[\left(\mu + \frac{\mu_t}{\sigma_{\varepsilon}} \right) \nabla \varepsilon \right] + \rho C_1 S \varepsilon \\ &- \rho C_2 \frac{\varepsilon^2}{k + \sqrt{\nu \varepsilon}} + C_{1\varepsilon} \frac{\varepsilon}{k} C_{3\varepsilon} G_b + S_{\varepsilon} \end{split} \tag{9}$$

The model constants [26] in Eqs. (8) and (9) are summarized in

The electric potential (V) can be defined through the electric field vector (E) by Gauss law as

$$\boldsymbol{E} = -\nabla V \tag{10}$$

The Poisson equation establishes a connection between the electric potential and the concentrations of charged species in the following manner:

Table 1 $\kappa - \varepsilon$ model constants

$\kappa - \varepsilon$ model	Constants	Values
	$C_{1arepsilon}$	1.44
Realizable	$C_{2arepsilon}$	1.90
	$C_{1arepsilon} \ C_{2arepsilon} \ C_{\mu}$	0.09
	σ_k	1.0
	$\sigma_arepsilon$	1.2
	S_k	UD
	$S_arepsilon$	UD

Note: User-defined (UD)

=

$$-\nabla^2 V = -\frac{\sum_i q_i e n_i}{\epsilon_0} \tag{11}$$

$$-\nabla^2 V = -q \frac{(n^+ - n^-)}{\epsilon_0} \tag{12}$$

where q_i and n_i represent the charge density and number density of species *i*, respectively. The permittivity of free space is denoted by the symbol ϵ_0 , which has a value that corresponds to 8.8542×10^{12} farad/m. Charge density, q is defined through the following equation:

$$q = \sum_{i=1}^{N} q_i = eN_a \rho \sum_{i=1}^{N} Y_i \frac{S_i}{\mathcal{M}_i}$$
 (13)

High voltage is used to power what has historically been referred to as "ionic wind" [27-29]. The body forces caused by the electric field are so significant at these energies that they affect the bulk velocity of the fluid. Nevertheless, in this work, only low voltages, $V \in$ [-5 V, +5 V], were utilized, and this has a number of significant repercussions for the modeling process. At these low voltages, the physics of semiconductors becomes most apparent; however, in this investigation, the physics is employed for sensing rather than actuation. So long as the low-voltage assumption is true, the bulk velocity, temperature distribution, and species distribution (except ions) will be unaffected by the applied voltage. The only processes that will be impacted are ion migration and recombination.

Chemical Kinetic Mechanism. The chemistry of ions in flames is described by combining the reactions of methane-oxygen flame with a 25-species reduced mechanism and the ionization reactions from Belhi et al. [14]. The reduced mechanism is obtained by employing a "Directed Relation Graph" with the error propagation method [30-32], using the opensource program pyMARS [33]. The magnitudes of the coefficients of the ionization reactions are shown in Table 2 [19]. For the charged species, the thermodynamic properties are retrieved from the Burcat database [34]. The transport properties are derived from Chen et al. [35].

The proton transfer reaction by formyl ion, HCO⁺, results in the production of the principal abundant cation, hydronium, H₃O⁺

$$CH + O \iff HCO^+ + e^-$$
 (R1)

$$HCO^{+} + H_{2}O \Longleftrightarrow H_{3}O^{+} + CO \tag{R2}$$

In the final step, a dissociative recombination reaction takes place, which recombines H_3O^+ with electrons (e^-) as follows:

$$H_3O^+ + e^- \Leftrightarrow H_2O + H$$
 (R3)

Despite the fact that other cations do form [36–39], H_3O^+ serves as the "source" of all subsequent cations and has the highest concentration. Essentially, H₃O⁺ and HCO⁺ represent the total quantity of positively charged species, as demonstrated by Belhi et al. [14]. Nevertheless, the rate at which H₃O⁺ is generated is on

Table 2 Arrhenius parameters for the ionization reaction mechanism

Reactions	Pre-exponential factor, A (cm ³ /mol s)	Temperature dependence, β	Activation energy, E_a (J/mol)
$CH + O \iff HCO^{+} + e^{-}$ $HCO^{+} + H_{2}O \iff H_{3}O^{+} + CO$ $H_{3}O^{+} + e^{-} \iff H_{2}O + H$	$2.512 \times 10^{11} \\ 1.0 \times 10^{16} \\ 1.44 \times 10^{17}$	$0 \\ -0.0897 \\ 0$	7.118×10^{3} 0 0

par with that of e^- . Furthermore, the HCO⁺ cation generates at a much slower pace than the e^- and H_3O^+ ions. Therefore, hydronium ion (H_3O^+) predominates in our study.

Modified Arrhenius equation is used to determine the reaction rates k for all reactions, as shown

$$k = AT^{\beta} e^{-\frac{E_a}{R_u T}} \tag{14}$$

where A denotes the Arrhenius pre-exponential factor, β stands for the temperature dependence, and E_a represents the activation energy.

The saturation potential is significantly impacted by the recombination reaction [39]. The rate of recombination can be determined using the equation

$$\frac{d[E]}{dt} = \frac{d[\text{ion}]}{dt} = -k \cdot [E][\text{ion}]$$
 (15)

It is conceivable that the value of electron mobility plays a significant part in determining the voltage at which saturation will take place. In this study, the electron mobility is $0.2 \text{ m}^2 \text{V}^{-1} \text{s}^{-1}$ [29] while the ionic (H_3O^+) mobility is $0.0018 \text{ m}^2 \text{V}^{-1} \text{s}^{-1}$ [6].

Electron species' mobility, diffusivity, space, and bulk velocity influence electric current density, while ion species' molar concentration determines ion current density. The following equations [4,40] are used to calculate current densities:

$$J_{\text{ion}} = -\sigma_{\text{ion}} K \nabla V - D \nabla \sigma_{\text{ion}} + \sigma_{\text{ion}} U$$
 (16)

$$J_e = \sigma_e K \nabla V - D \nabla \sigma_e + \sigma_e U \tag{17}$$

In Eqs. (16) and (17), $\sigma_{\text{ion}}(=qN_ac_{\text{ion}})$ and $\sigma_e(=qN_ac_e)$ are the space charge densities for ions and electrons, respectively. In

addition, the Nernst–Einstein relation is used to determine the value of the molecular diffusivity (D)

$$D_i = \frac{k_i k_B T}{q_e} \tag{18}$$

Initial and Boundary Conditions. To initiate and maintain stable combustion in the steady-state simulation, the solution was initialized in a particular manner following certain thought-out steps. This was done to ensure that combustion would start without the need for introducing high-temperature patches in the domain to mimic artificial ignition. First, the entire domain is initiated at standard air composition at Standard temperature and pressure with the fuel inlet temperature set to 1500 K. Then, a partially converged solution is obtained by neglecting the enthalpy gain from chemical reactions. This sets up a partially converged flow field and species distribution in the domain. The high temperature (1500 K) gas flow from the inlet also establishes an approximate flame profile in the domain. Once this partial solution is obtained, the fuel inlet temperature is set back to the actual value (600 K), and the enthalpy gain from the chemical reactions is no longer neglected in the energy equation. Since a high-temperature flame profile has already been setup in the domain, combustion initiates without the need to introduce high-temperature patches that tend to cause numerical instabilities.

The 3D domains' boundary conditions are consistent with the experimental demonstrations from Martin et al. [1,15]. Referring to Fig. 3, the work surface temperature is assigned to be 600 K and is compatible with the experiment's preheating procedure. In addition, the surface of the torch is regarded to be at the same temperature, which is 600 K. An inlet velocity of 28 ms $^{-1}$ and a fuel-oxygen (F/O) ratio of 0.833 (i.e., $\chi_{\rm CH_4}=0.45$, and $\chi_{\rm O_2}=0.55$) were specified for

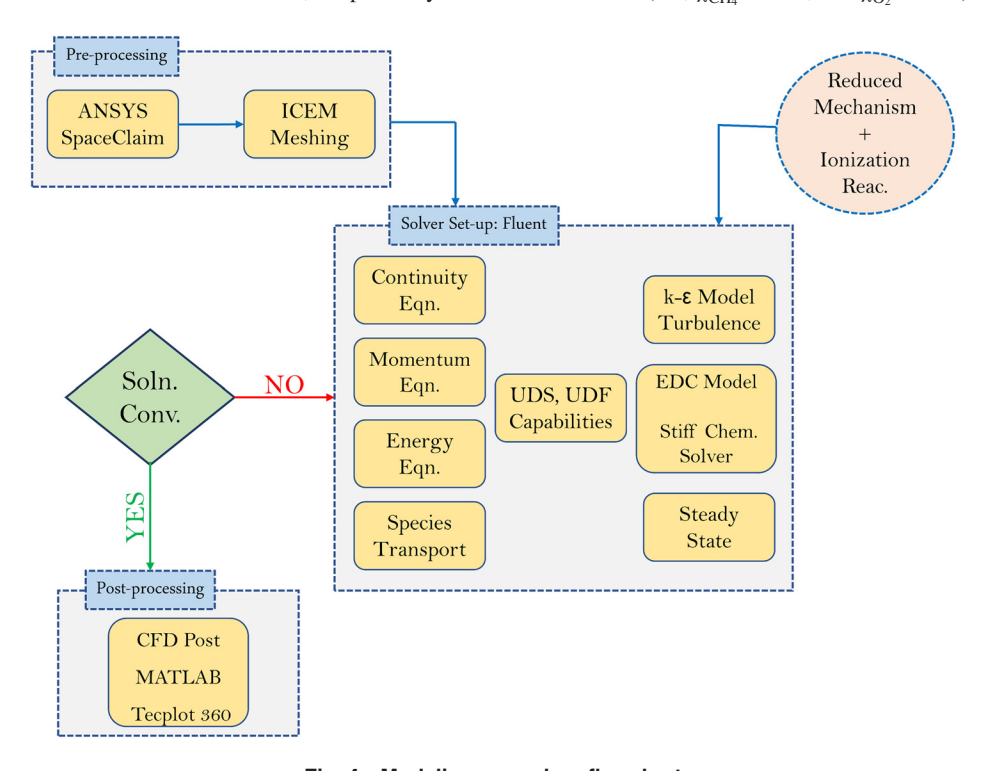


Fig. 4 Modeling procedure flowchart

the delivery of the fuel-oxygen mixture. The work surface is considered to be at ground potential while a range of voltages, $V \in [-5\,\mathrm{V}, +5\,\mathrm{V}]$, is applied to the torch. To ensure that the boundary condition does not impact flow upstream, the domain's outer boundaries that open to ambient air, are treated as "Outflow" boundaries assuming a zero-diffusion flux normal to the boundary for all variables.

Computational Procedure. A 3D computational fluid dynamics (CFD) model was developed using ansity Fluent 2022R1. The governing equations are solved using a finite volume technique. For the purpose of discretizing the governing equations across the entire domain, a spatial discretization method of the second order was chosen. For the purpose of solving the governing equations, the coupled pressure–velocity coupling algorithm was utilized. The pressure equation was solved using the PRESTO! scheme. As a result of the turbulent nature of the flow in the domain, the realizable $\kappa - \varepsilon$ turbulence model was selected to represent the viscosity. In order to deal with the turbulence-chemistry interaction, a stiff chemistry solver and the eddy dissipation concept were both introduced to the CFD code. The convergence criterion for the equations' residual term is finally fixed to 1×10^{-5} . The modeling technique is illustrated in Fig. 4.

The discretization error was estimated by a grid convergence study utilizing Richardson extrapolation [41]. The articles from Refs. [24] and [42–45] detail recent applications of such a method.

The investigation into the grid convergence index is illustrated by a spider plot, which can be found in Fig. 5. Temperature, velocity, and electric potential are the three characteristics that have been taken into consideration at various places throughout the three-dimensional domain and have subsequently been enumerated for a variety of grid sizes. When compared to the values that were acquired with a finer mesh, the results that were produced with a medium mesh ($\approx 1.6 \times 10^6$ elements) appeared to be within the margin of error, which was a tradeoff for the increased computational expense and the acquisition of appropriate outcomes.

Figure 6 shows the surface meshing (hexahedral) for the 3D model performed in ansys icem CFD and the total element count for this mesh is $\approx 1.6 \times 10^6$. The inflation layer near work surface was about $\approx 1 \, \mu \text{m}$ as shown in Fig. 6(b).

While the convergence of the computational model was tracked using the $y^+ \equiv \frac{u_* y}{\nu}$ value, the Debye length played a pivotal role in the electrical transport portion of this investigation. The Debye length [15,22] is thus determined to ensure that the meshes are adequately resolving the electrical species

$$\lambda_D = \sqrt{\frac{\frac{\varepsilon_0 k_B}{q_e^2}}{\frac{n_e}{T_e} + \sum_{i}^{N} \frac{z_i^2 n_i}{T_i}}}$$
(19)

where the Debye length is denoted by λ_D , n_e is the density of electrons, T_e and T_i are the temperature of the electrons and ions,

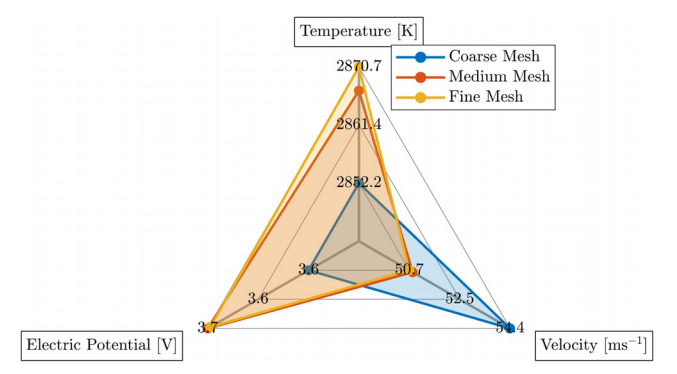
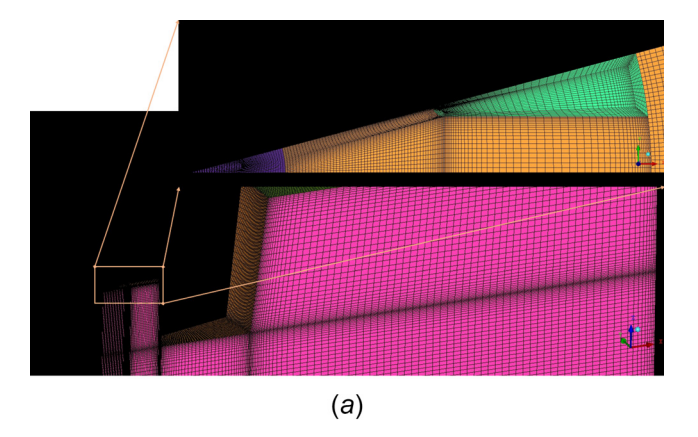


Fig. 5 Grid convergence index spider plot



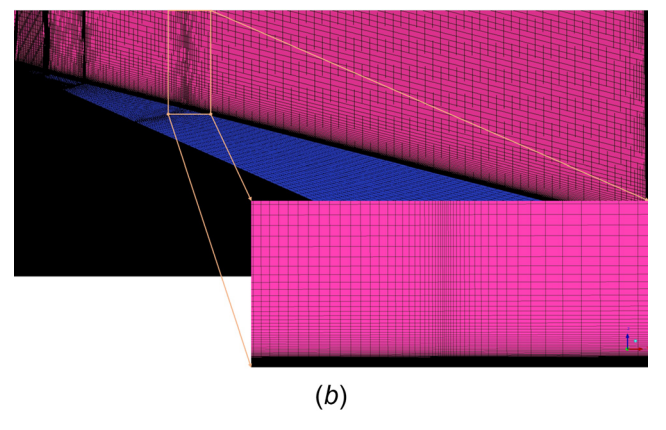


Fig. 6 Surface meshing over 15 deg wedge model: (a) meshing in inlet region and (b) inflation layer near work surface

respectively, z_i is the rate of ionic charge relative to electron charge, n_i is the density of atomic species i. Clements and Smy's assumption [46,47] assumes that the temperature of electrons and ions is the same as the temperature of the flame $(T_e \approx T)$.

Results and Discussions

For the purpose of tracing the axial distribution of the combustion and electrochemical parameters, somewhat virtual flame inspection lines were created in the 3D domain.

Premixed CH₄–O₂ Flame. Because the molar fractions of electrons and ions in the flow are relatively small, it is assumed that electron and ion transportation does not alter the velocity and temperature profiles of the flow when the voltage is at a low level.

In the three-dimensional domain, the flame produced by premixed methane and oxygen burns in a triangle pattern. Figure 7 depicts the

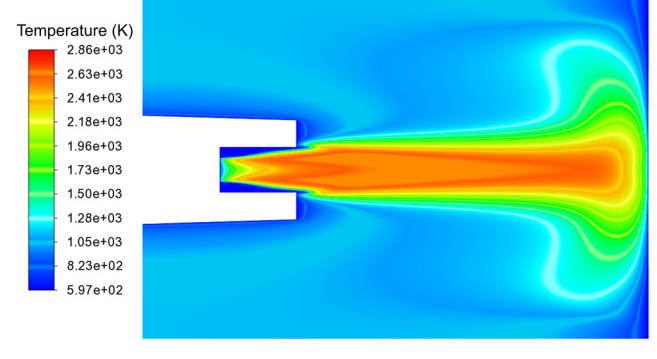


Fig. 7 Temperature contour plot taken from the cross section of the 15 deg wedge model

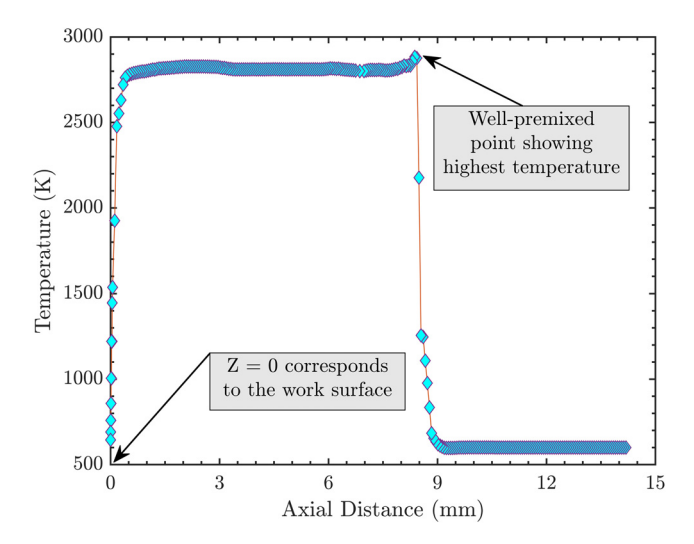


Fig. 8 Axial distribution of temperature along virtual flame line. The flame line is a vertical construction line from the torch tip to the work surface (plate).

temperature contour plot in the vicinity of the torch tip. Additionally, it can be seen from the profile that the temperature is relatively high directly below the triangular slit.

There is not an onset hint of a change in temperature when the electric field is generated, and that is because the unburned gas is not being affected. The temperature, on the other hand, has not changed at all. Ion mobility increases with an increase in temperature, although it is still at least two orders of magnitude lower than that of electron mobility.

Figure 8 is an illustration of the temperature profile as it is distributed axially. As can be observed, the area in which the fuel (CH_4) and air (O_2) mixture is well premixed is the region with the maximum temperature. Because the area near the torch tip is devoid of electrons, currents have to be carried by heavy positive ions that are forced upstream against the flow.

The velocity contour plot over the domain is depicted in Fig. 9. The sudden release of heat and subsequent expansion of the flue gases (of reaction) both have a sizeable effect on the velocity field and result in flow patterns that are strikingly unlike those that would be anticipated for a flow that is not reacting. In addition, if the velocity in the reaction zone is too low, this will give the ions in the outer cone more time to recombine. As a direct consequence of this, ion concentrations are reduced, as are the resulting saturation currents.

Electrons and Ions Distribution. The generation rate of e^- is displayed in Fig. 10 and has a maximum value of 0.00204 Kmol/ m^3 s. When an electric bias voltage that is sufficiently strong is

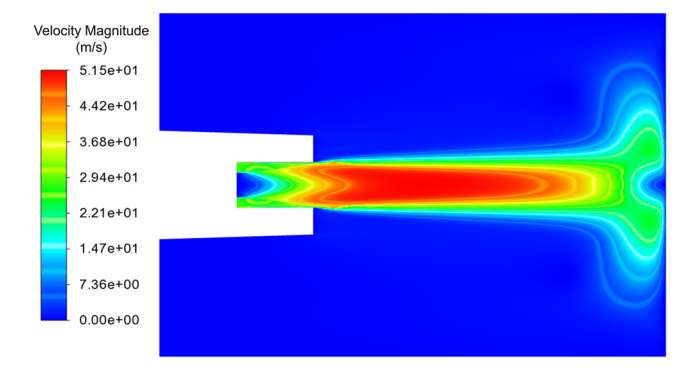


Fig. 9 Velocity contour plot taken from the cross section of the 15 deg wedge model

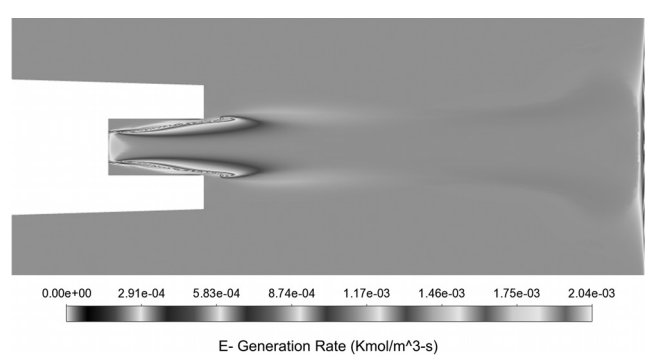


Fig. 10 Generation rate of e⁻ taken from the cross section of the 15 deg wedge model

supplied, the charge carriers can be pushed away to the area close to the absorbing surfaces. Because free electrons are transported quickly in the gas phase, the metal surfaces are able to absorb them, resulting in the production of a positively charged "sheath" [48]. The sheath is the region near the surface that has considerable variances in the quantity of ions and electrons, which subsequently causes an electrical potential difference. This region is located near the surface.

A contrast between the two scenarios is depicted in Fig. 11; in the first case, an electric field is not being applied, while in the second, a potential difference of 5 V is. When an electric field is present, it is interesting to view that the peak value of the principal charge carrier $\rm H_3O^+$ is reduced. This can be understood by considering the fact that in this hypothetical situation, charged species are extracted from the reaction zone.

Because of the greater magnitude of the electric potential, there is a greater concentration of the positively charged hydronium ion (H_3O^+) . Due to the fact that the concentration of HCO^+ is low, it undergoes an almost instantaneous transformation into H_3O^+ in accordance with Reaction R2. The molar concentration of H_3O^+ demonstrated in Fig. 12 depicts such criteria.

Concentrations of positive ions are slightly higher when the interaction between electrons and negative ions is disregarded, as in the case of the recombination of electrons with the $\rm H_3O^+$ ion (see Reaction R3). On the other hand, a higher recombination reaction rate would indicate that a greater percentage of charged particles are reacting to become neutrals, which results in a decreased number of charged particles that may be collected at the surfaces.

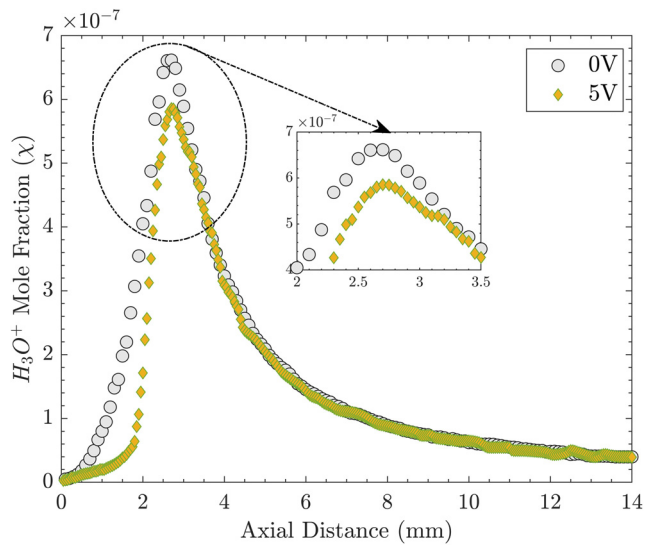


Fig. 11 H₃O⁺ mole fraction distributed axially

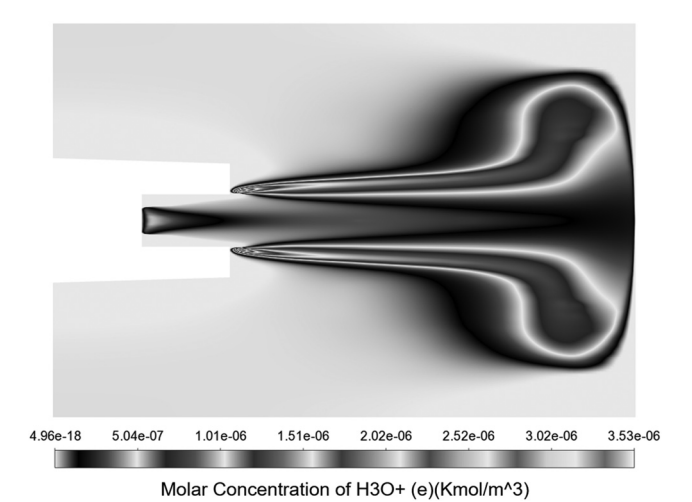


Fig. 12 Molar concentration of ${\rm H_3O^+}$ taken from the cross section of the 15 deg wedge model

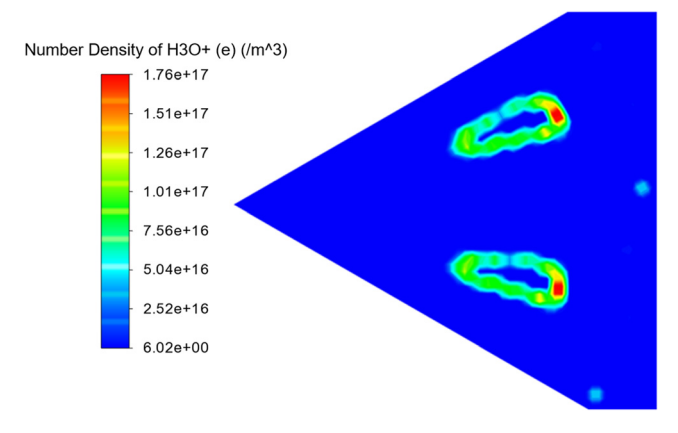


Fig. 13 Number density of $\rm H_3O^+$ taken at a slice of $\it Z = 2.0\,\rm mm$ from the torch tip

The cross-sectional average current density does not change across the domain in general. Figure 13 illustrates the color contour pattern for the number density associated with ${\rm H_3O^+}$. In order to facilitate a deeper level of comprehension, the angle of the geometry was adjusted to 60 deg by mirroring the periodic faces (Fig. 3). The number density profiles of electrons and ions are generated as a result of running the electrical species transport model. As can be seen, the highest magnitude of species number density is $10^{17}/{\rm m}^3$, and this is somewhat different from the actual measurement, which is $10^{18}/{\rm m}^3$ [6]. At the surface of the torch, the concentration of ${\rm H_3O^+}$ begins to decrease when a positive voltage is applied, however, the concentration of ${\rm H_3O^+}$ continues to be considerable at the work surface. Due to the fact that the electron is moving upstream while ${\rm H_3O^+}$ is not, a pocket of e^- concentration is created.

Electrical Characteristics. An electric field flows from the negative to the positive terminal, and electrons move in the opposite direction of positive ions, in accordance with the laws of electricity. The presence of the electric field has a significant impact on the manner in which the flame behaves. Whenever an electric field (Fig. 14) is applied, the maximal concentrations of cations and electrons shift closer to the positive terminal. This occurs because the cations and electrons are drawn to the field. Because of the disparity in the numbers of ions and electrons, sheaths can be seen forming on both the torch and the work surface. Based on these findings, it appears that the grid was successful in resolving the Debye length.

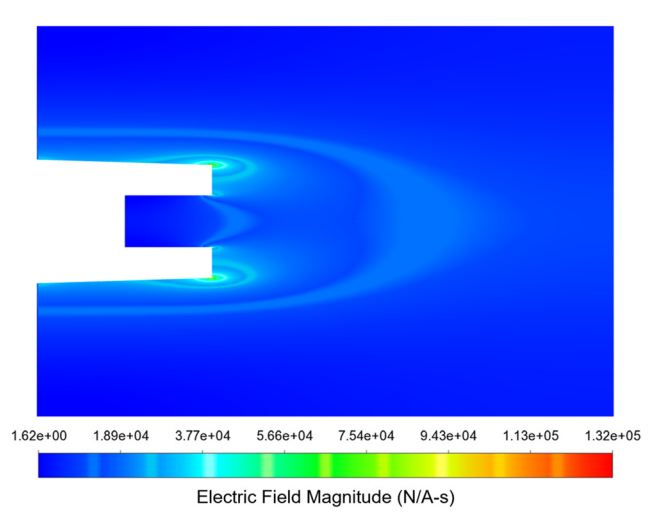


Fig. 14 Magnitude of electric field taken from the cross section of the 15 deg wedge model

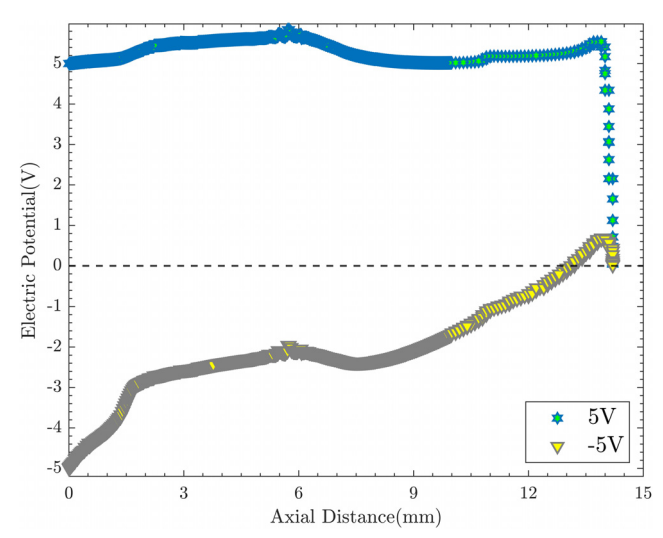


Fig. 15 Axially distributed electric potential along virtual flame line

As a result of the fact that the effect of the ionic wind has not been taken into account at low voltages, the potential of the flame is virtually the same throughout. It has a substantially higher level of electrical conductivity because there is a significantly higher concentration of ions at the front of the flame than there is anywhere else in the flame. This suggests that it builds a conductive bridge between the plasma in the outer cone below and the torch tip.

When a positive voltage, such as +5 V, is provided at the torch tip, the electric potential does not decrease proportionally due to the presence of a high density of the electrical species. This can be seen clearly in Fig. 15. Nevertheless, if the voltage is negative, such as -5 V, the gradients might be perceived close to the work surface. This is referred to as saturation. The more mobile of the two charge carriers, e^- , leaves the region near the negative surface, which results in the growth of the sheath. The only way to further enhance current is to increase the transport of the less mobile charge carrier, H_3O^+ , via the sheath. However, this process is exceedingly sluggish in comparison to e^- , and as a result, the current only increases very slowly with increasing voltage. In addition, when a negative voltage is supplied, a substantial voltage drop can be seen, as depicted in Fig. 15. It is hypothesized that this is because of the ohmic losses that occur along the length of the flame.

i–v characteristics. To illustrate how an electric field affects a premixed oxyfuel flame, Fig. 16 shows the i–v characteristics of the

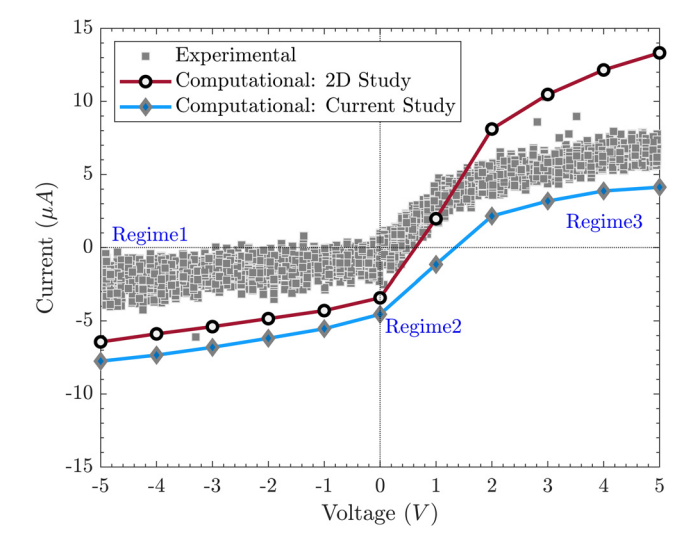


Fig. 16 Current-voltage (i-v) characteristics

flame. At various electric bias voltages, the i– ν curve transitions through three distinct phases.

In regime 1, the flame experiences a partial saturation state. Although Ohm's law remains applicable, the availability of electrons upstream of the flame becomes depleted. As a result, the current flow is constrained by the capacity to draw positive ions against the flow within the narrow gap between the flame and the torch tip. While this can still be achieved due to the small distance involved, these currents diminish rapidly as the flame begins to lift off from the tip.

As shown, Fig. 16 depicts the i–v curve with its three distinct regimes. Since the standoff (torch tip-to-work surface distance) is high and the signals are weak, the experimental curve shows a lot of scatters. Figure 16 clearly displays the linear agreement between the experimental and computational models in regime 1. Since there are fewer electrons in the region around the torch's tip, currents carried by heavy positive ions are forced upstream, against the flow. On the contrary, regime 3 exhibits a few distinguishing characteristics to a certain extent [49,50]. Possible explanations for why there is such a difference in results include the following:

- (I) Multiplying the ion concentration by the average velocity and the average flame area yields the current in regime 3. As can be seen, the ion concentration in Fig. 13 is an order of magnitude lower than what was found in the experiment. In addition, regime 3 has a strong velocity sensitivity. With decreasing velocity, the regime 3 current will tend to decline.
- (II) Negative voltages don't affect i-v relationship or saturation voltage due to electron mobility. Nonetheless, positive saturation voltages are inversely related to electron mobility. Consequently, the mobility of ions has a significant impact. Since ion mobility is fairly low, the recombination rate plays a larger role. With increasing recombination, a greater proportion of charged particles will undergo neutralization reactions.

Conclusions

A simplified 3D model of an oxyfuel premixed (CH_4-O_2) flame's preheating step was developed using ANSYS FLUENT CFD code. The preceding findings allow for a few interpretations. In this process, charged "sheaths" are produced on both the torch and the workpiece, leading to three distinct regimes in the i-v relationship. The ions will have more time to recombine in the outer cone if the velocities in the hot zone are extremely low. This leads to decreased ion concentrations and saturation currents. Regime 2 highlights the significance of flame resistance in determining the standoff distance. In regime 3, positive saturation currents play a crucial role in detecting chemical

activity on the work surface. In regime 1, "partial" saturation of the flame is observed, and as such, the F/O ratio and flow rate have a significant influence. This study provides the aforementioned insights, allowing for the development of a reliable computational model that facilitates the exploration of factors that are difficult to measure directly. The validation of such a tool could yield valuable insights for the design of new torch tips, enhancing specific aspects of the signal in regime 1.

Funding Data

 National Science Foundation (NSF) (Award Nos.: 1900540 and 1900698; Funder ID: 10.13039/100000001).

Conflict of Interest

The authors declare that they have no known competing financial interests or personal relationships that could have appeared to influence the work reported in this paper.

Data Availability Statement

The datasets generated and supporting the findings of this article are obtainable from the corresponding author upon reasonable request.

Nomenclature

```
c_i = \text{molar concentration of species } i, \text{ Kmol m}^{-3}
```

 $D_i = \text{diffusivity of species } i, \, \text{m}^2 \, \text{s}^{-1}$

 $E_a = activation energy, J mol^-$

k = rate constant

 $K = \text{mobility, m}^2 \text{ V}^{-1} \text{ s}^{-1}$

 $k_B = \text{Boltzmann constant } (1.38 \times 10^{-23}), \text{ J K}^{-1}$

MW = molecular weight

 n_i = number density of species i, m⁻³

 $P = \text{density}, \text{kg/m}^3$

 q_e = fundamental charge (1.6 × 10⁻¹⁹), C

 $R_u = \text{universal gas constant (8.314), J mol}^{-1} \text{ K}^{-1}$

t = time, sec

T =temperature, K

 $U = \text{velocity, ms}^{-}$

 $Y_i = \text{mass fraction of species}, i$

 β = temperature exponent

 $\epsilon_0 = \text{vacuum permittivity } (8.9 \times 10^{-12}), \text{ C V}^{-1} \text{ m}^{-1}$

 λ_D = Debye length, μ m

 σ_i = space charge density of species i, C m⁻³

References

- Martin, C. R., 2017, "Mechanized Oxyfuel Control With Ion Current Sensing," Weld. J., 96(5), pp. 154–162.
- [2] Martin, C. R., 2017, "Replacing Mechanized Oxyfuel Cutting Sensors With Ion Current Sensing," ASME Paper No. MSEC2017-2789.
- [3] Martin, C. R., 2018, "Work Piece Condition Detection Using Flame Electrical Characteristics in Oxy-Fuel Thermal Processing Equipment," U.S. Patent No. 10067496.
- [4] Xu, K., Untaroiu, A., and Martin, C. R., 2020, "Simulation of Ion Current in Oxyfuel Flame Subject to an Electric Field," ASME Paper No. IMECE2020-24601.
- [5] Martin, C. R., Untaroiu, A., and Xu, K., 2021, "A One Dimensional Model for Ion Transport in a Flame With Two Absorbing Surfaces," Combust. Theory Modell., 25(1), pp. 22–43.
- [6] Martin, C. R., Untaroiu, A., and Xu, K., 2022, "Spatially Resolved Ion Density Measurements in an Oxyfuel Cutting Flame," Combust. Sci. Technol., 194(5), pp. 930–945.
- [7] Wilson, H., 1916, "The Electrical Conductivity and Luminosity of Flames Containing Salt Vapours," Philos. Trans. R. Soc. Lond., 216, pp. 63–90.
- [8] Calcote, H. F., 1961, "Ion Production and Recombination in Flames," Symp. (Int.) Combust., 8(1), pp. 184–199.
- [9] Lawton, J., and Weinberg, F. J., 1969, Electrical Aspects of Combustion, Clarendon Press, Oxford.
- [10] Fialkov, A. B., 1997, "Investigations on Ions in Flames," Prog. Energy Combust. Sci., 23(5–6), pp. 399–528.

- [11] Han, J., Belhi, M., Casey, T. A., Bisetti, F., Im, H. G., and Chen, J.-Y., 2017, "The i–v Curve Characteristics of Burnerstabilized Premixed Flames: Detailed and Reduced Models," Proc. Combust. Inst., 36(1), pp. 1241–1250.
- [12] Pond, T. L., and Martin, C. R., 2020, "Electrical Characteristics of the Oxyfuel Flame While Cutting Steel," Exp. Therm. Fluid Sci., 112, p. 109985.
- [13] Martin, C. R., Untaroiu, A., Xu, K., and Rahman, S. M. M., 2022, "A Study of the Efficacy of Flame Electrical Resistance for Standoff Measurements During the Oxyfuel Cutting Process," ASME J. Manuf. Sci. Eng., 144(7), p. 071010.
- [14] Belhi, M., Domingo, P., and Vervisch, P., 2010, "Direct Numerical Simulation of the Effect of an Electric Field on Flame Stability," Combust. Flame, 157(12), pp. 2286–2297.
- [15] Martin, C. R., 2018, "A Study of Ion Currents in an Oxyfuel Flame Due to Work Surface Chemical Action," Exp. Therm. Fluid Sci., 98, pp. 239–250.
- [16] Goodings, J. M., Guo, J., Hayhurst, A. N., and Taylor, S. G., 2001, "Current-Voltage Characteristics in a Flame Plasma: Analysis for Positive and Negative Ions, With Applications," Int. J. Mass Spectrom., 206(1–2), pp. 137–151.
- [17] Karnani, S., and Dunn-Rankin, D., 2015, "Detailed Characterization of DC Electric Field Effects on Small Non-Premixed Flames," Combust. Flame, 162(7), pp. 2865–2872.
- [18] Imamura, O., Chen, B., Nishida, S., Yamashita, K., Tsue, M., and Kono, M., 2011, "Combustion of Ethanol Fuel Droplet in Vertical Direct Current Electric Field," Proc. Combust. Inst., 33(2), pp. 2005–2011.
- [19] Speelman, N., de Goey, L. P. H., and van Oijen, J. A., 2015, "Development of a Numerical Model for the Electric Current in Burner-Stabilised Methane–Air Flames," Combust. Theory Modell. 19(2), pp. 159–187.
- Flames," Combust. Theory Modell., 19(2), pp. 159–187.
 [20] Luo, Y., Gan, Y., and Jiang, Z., 2020, "Study on the Electrical Response of Small Ethanol-Air Diffusion Flame Under the Uniform Electric Field," Int. J. Energy Res., 44(14), pp. 11872–11882.
- [21] Martin, C. R., Pond, T., Tomas, J., Schmit, J., Miguel, E., Untaroiu, A., and Xu, K., 2020, "Semiconductor Aspects of the Oxyfuel Cutting Torch Preheat Flame: Part II—The Flame's Internal Electrical Structure," ASME Paper No. MSEC2020e250
- [22] Xu, K., 2021, "Simulation of Electrical Characteristics in Oxyfuel Flame Subject to an Electric Field," M.S. thesis, Virginia Tech, Blacksburg, VA.
- [23] Law, C. K., 2006, Combustion Theory, 2nd ed., CRC Press, Boca Raton, FL
- [24] Untaroiu, A., Rahman, S. M. M., and Martin, C. R., 2023, "Role of Secondary Ions on the i–v Characteristics of Oxyfuel Flame Subject to an Electric Field," ASME J. Fluids Eng., 145(7), p. 071202.
- [25] Shih, T. H., Liou, W. W., Shabbir, A., Yang, Z., and Zhu, J., 1995, "A New k ε Eddy Viscosity Model for High Reynolds Number Turbulent Flows," Comput. Fluids, 24(3), pp. 227–238.
 [26] ANSYS, 2013, "ANSYS Fluent User's Guide," ANSYS FLUENT 12.0 User's
- [26] ANSYS, 2013, "ANSYS Fluent User's Guide," ANSYS FLUENT 12.0 User's Guide, accessed July 20, 2023, https://www.afs.enea.it/project/neptunius/docs/fluent/html/ug/main_pre.htm
- [27] Farraj, A. R. D., Al-Naeemy, A. M., Al-Khateeb, A. N., and Kyritsis, D. C., 2017, "Laminar Non-Premixed Counterflow Flames Manipulation Through the Application of External Direct Current Fields," J. Energy Eng., 143(4), p. 04017002.
- [28] Belhi, M., Han, J., Casey, T. A., Chen, J.-Y., Im, H. G., Sarathy, S. M., and Bisetti, F., 2018, "Analysis of the Current–Voltage Curves and Saturation Currents in Burner Stabilised Premixed Flames With Detailed Ion Chemistry and Transport Models," Combust. Theory Modell., 22(5), pp. 939–972.
- [29] Belhi, M., Lee, B. J., Cha, M. S., and Im, H. G., 2019, "Three-Dimensional Simulation of Ionic Wind in a Laminar Premixed Bunsen Flame Subjected to a Transverse dc Electric Field," Combust. Flame, 202, pp. 90–106.
- [30] Lu, T., and Law, C. K., 2005, "A Directed Relation Graph Method for Mechanism Reduction," Proc. Combust. Inst., 30(1), pp. 1333–1341.

- [31] Desjardins, P. P., and Pitsch, H., 2008, "An Efficient Errorpropagation- Based Reduction Method for Large Chemical Kinetic Mechanisms," Combust. Flame, 154(1-2), pp. 67–81.
- [32] Niemeyer, K. E., and Sung, C.-J., 2011, "On the Importance of Graph Search Algorithms for DRGEP-Based Mechanism Reduction Methods," Combust. Flame, 158(8), pp. 1439–1443.
- [33] Mestas, III, P. O., Clayton, P., and Niemeyer, K. E., 2019, "pyMARS: Automatically Reducing Chemical Kinetic Models in Python," J. Open Source Software, 4(41), p. 1543.
- Software, 4(41), p. 1543.
 [34] Burcat, A., 2006, "Ideal Gas Thermodynamic Data in Polynomial Form for Combustion and Air Pollution Use," Budapest, Hungary, accessed Nov 11, 2022, http://garfield.chem.elte.hu/Burcat/burcat.html
- [35] Chen, B., Wang, H., Wang, Z., Han, J., Alquaity, A. B. S., Wang, H., Hansen, N., and Sarathy, S. M., 2019, "Ion Chemistry in Premixed Rich Methane Flames," Combust. Flame, 202, pp. 208–218.
- [36] Goodings, J. M., Bohme, D. K., and Ng, C.-W., 1979, "Detailed Ion Chemistry in Methane-Oxygen Flames. I. Positive Ions," Combust. Flame, 36, pp. 27–43.
- [37] Fialkov, A. B., Kalinich, K. Y., and Fialkov, B. S., 1992, "Experimental Determination of Primary Ions in Flame," Symp. (Int.) Combust., 24(1), pp. 785–791.
- [38] Pedersen, T., and Brown, R. C., 1993, "Simulation of Electric Field Effects in Premixed Methane Flames," Combust. Flame, **94**(4), pp. 433–448.
- [39] Prager, J., Riedel, U., and Warnatz, J., 2007, "Modeling Ion Chemistry and Charged Species Diffusion in Lean Methane Oxygen Flames," Proc. Combust. Inst., 31(1), pp. 1129–1137.
- [40] Belhi, M., Lee, B. J., Bisetti, F., and Im, H. G., 2017, "A Computational Study of the Effects of dc Electric Fields on Non-Premixed Counterflow Methane-Air Flames," J. Phys. D Appl. Phys., 50(49), p. 494005.
- [41] Celik, I. B., Ghia, U., Roache, P. J., and Freitas, C. J., 2008, "Procedure for Estimation and Reporting of Uncertainty Due to Discretization in CFD Applications," ASME J. Fluids Eng., 130(7), p. 078001.
- [42] Alam, M. D., and Soeimanikutanaei, S., 2021, "Effects of Geometrical Configuration on the Aerodynamic Performance of the Joined Wings," ASME Paper No. IMECE2021-72087.
- [43] Alam, M. D., and Cao, Y., 2021, "Static and Modal Analysis of a Crankshaft Reciprocating Driver for Reciprocating-Airfoil (RA) Driven VTOL Aircraft," Mech. Based Des. Struct. Mach., 51(9), pp. 5072–5087.
 [44] Fu, G., and Untaroiu, A., 2021, "Investigation of Tire Rotating
- [44] Fu, G., and Untaroiu, A., 2021, "Investigation of Tire Rotating Modeling Techniques Using Computational Fluid Dynamics," ASME J. Fluids Eng., 143(11), p. 111206.
- [45] Hayden, A., and Untaroiu, A., 2022, "Strain Response and Aerodynamic Damping of a Swirl Distortion Generator Using Computational Fluid Dynamics," ASME J. Fluids Eng., 144(3), p. 031204.
- [46] Clements, R. M., and Smy, P. R., 1969, "Electrostatic-Probe Studies in a Flame Plasma," J. Appl. Phys., 40(11), pp. 4553–4558.
- [47] Clements, R. M., and Smy, P. R., 1970, "Ion Current From a Collision-Dominated Flowing Plasma to a Cylindrical Electrode Surrounded by a Thin Sheath," J. Appl. Phys., 41(9), pp. 3745–3749.
- [48] Boucher, P. E., 1928, "The Drop of Potential at the Cathode in Flames," Phys. Rev., 31(5), pp. 833–850.
- [49] Martin, C. R., Oswald, D., Rahman, S. M. M., and Untaroiu, A., 2023, "Ions in the Oxyfuel Cutting Flame Due to Workpiece Carbon," Manuf. Lett., 36, pp. 22–25.
- [50] Rahman, S. M. M., Warrier, R., Untaroiu, A., and Martin, C. R., 2022, "Electrical Characteristics of the Oxyfuel Preheat Flame: 3D Computational Model Subject to Electric Bias Voltages," ASME Paper No. IMECE2022-95787.